Aeroacoustic Boundary Element Method Using Analytical/Numerical Matching

Ronald J. Epstein* and Donald B. Bliss†
Duke University, Durham, North Carolina 27708-0300

A unified aeroacoustic boundary element theory has been formulated using analytical/numerical matching (ANM). ANM is a hybrid scheme combining a low-resolution global numerical solution with high-resolution local solutions to form a composite solution. ANM is applied to problems in unsteady aerodynamics and aeroacoustics. This includes both two and three dimensions for lifting surfaces in unsteady, compressible, irrotational flow to calculate the unsteady aerodynamic loading and the associated acoustic field. The solution procedure utilizes overlapping smoothed doublets and local corrections to calculate the doublet strength distribution on the surface of the boundary in question. In ANM, a smoothing length scale is introduced that is larger than the length scale of numerical discretization and smaller than the largest physical scale. The global low-resolution solution is calculated numerically using smoothed doublet solutions to the convective wave equation, and it converges quickly. Local corrections are done with high-resolution analytical solutions. The global numerical solution is asymptotically matched to the local analytical solutions via a matching solution. The matching solution cancels the global solution in the near field, and cancels the local solution in the far field. The ANM composite solution gives both the surface pressure distribution and the radiated acoustic field. The method is very robust, offering insensitivity to control point location. No explicit wake geometry is assumed; therefore, a fixed or free wake model can be used. ANM provides high-resolution calculations from low-resolution numerics with analytical corrections, while avoiding the subtlety involving singular integral equations, and their numerical implementation.

Nomenclature

A_{kj}, B_{kj}, D_{kj}	= influence coefficient arrays
a_∞	= speed of sound
b	= subscript to denote body
C	= chord
c_0	= edge constant 1
c_1	= edge constant 2
D	= phase radius
D_s	= smoothed phase radius
d_s	= doublet spacing
H_n^m	= Hankel function of the mth kind of order n
k	= freespace wave number, ω/a_∞
k_r	= reduced frequency, $\omega C/2U_\infty$
$\mathcal{L}$	= local solution
M	= Mach number, U_∞/a_∞
$\mathcal{M}$	= matching solution
n	= normal coordinate direction
p	= point in space (x, y, z)
$\boldsymbol{p}$	= position vector
R	= amplitude radius
R_s	= smoothed amplitude radius
r	= $[(x/\beta)^2 + r_c^2]$
r_c	= smoothing length scale
S	= surface
S_{mod}	= subsurface
t	= time
U_∞	= freestream velocity
v_n	= normal velocity
$\bar{v}_n$	= harmonic normal velocity
w	= subscript to denote wake
x, y, z	= field point Cartesian coordinates
β	= $(1 - M^2)$
γ	= $M/\beta = M/(1 - M^2)$
$\Delta \boldsymbol{r}$	= change in position vector
θ	= $\arctan(\beta r_c / x)$
λ	= wavelength
μ	= doublet strength density
ξ, η, ζ	= source point Cartesian x, y, and z, coordinates, respectively
σ	= source strength density
τ	= D/a_∞
τ_s	= smoothed phase radius
φ	= velocity potential
$\bar{\varphi}$	= harmonic velocity potential
ω	= frequency

I. Introduction

PANEL methods,[1] or singularity methods, are a cornerstone of modern aerodynamic analysis. These methods construct aerodynamic flowfields from the superposition of simple building-block solutions of the governing equations distributed over the body surfaces. The appropriate strengths of these elementary solutions are determined by the application of surface boundary conditions. Panel methods are used to analyze compressible, steady and unsteady, potential flow over wings and bodies for a variety of applications including: performance, loads analysis, aeroacoustics, aeroelasticity, vibration, and interactional and interference effects.

Although these methods have been in use for a number of years, and have been the subject of much research and refinement, they possess significant shortcomings. Zero thickness lifting surface methods can be very sensitive to the location of the control points at which the boundary conditions are applied. Certain rules, such as the well-known $\frac{1}{4}-\frac{3}{4}$ chord rule for vortex lattice, must be strictly adhered to or incorrect answers will result.[2] Panels must be of regular shape and arrangement, partly because of this sensitivity. Problems may arise when panel sizes or orientations vary rapidly, when panels must also be compatible with a separate grid for structural analysis, and when other surfaces or wakes are in close proximity. Many of these problem have been addressed with higher-order panel techniques,[3–5] however, only in the context of steady aerodynamics. The analysis of free wakes by these methods poses a particular problem because

wake motion leads to irregular distortion of the constituent panels, and their proximity and orientation relative to other panels on aerodynamics surfaces is difficult to anticipate. Another limitation is that steady and unsteady loading contributions must be handled by separate means and that unsteady analysis is typically restricted to the frequency domain for compressible flow. Finally, there are other difficulties and subtleties associated with their implementation. In general, these methods are the numerical embodiment of a singular integral equation having a kernel function whose discretization is open to interpretation, leading to possible ambiguity in the meaning of computed results.

This paper presents a novel aeroacoustic boundary element method. The solution methodology is a unified approach to aeroacoustics. Unlike many other popular aeroacoustic computational schemes, the methodology presented does not involve a patchwork of different computational methods, e.g., a local computational fluid dynamic solution (finite difference scheme, or finite element scheme) patched to a Kirchhoff acoustic radiation calculation. The entire calculation is unified. This consistent aeroacoustic treatment is achieved by our novel boundary elements themselves. The fundamental element used in the method includes the physics of both the acoustics and the fluid dynamics. This results in a consistent formulation of the aeroacoustic problem, within the framework of a relatively simple model. In fact, free wake effects can be included in the model with only slight modifications in the methodology itself.

The methodology is simple and as presented for flat plate and rectangular wing aerodynamics is not intended to offer an immediately viable solution methodology for the aerospace industry; however, we believe the method has potential for future development and eventually may provide an efficient design tool. The methodology is easily extensible to include thickness effects and also can be used in conjunction with a structural analysis methodology (finite element method or some other scheme) to include blade structural dynamics. Presently, work is underway for a time domain version of the scheme.

As such, the present research involves a novel and innovative reformulation of the fundamental approach to singularity methods, with the goal of alleviating some of the shortcomings and difficulties associated with the traditional approach. The basis for this reformulation is a new analysis technique called analytical/numerical matching (ANM).

II.   ANM

ANM[6-14] is a hybrid technique that combines analytical and numerical solutions by a matching procedure. ANM allows a global low-resolution numerical solution and a local high-resolution analytical solution to be combined formally by asymptotic matching to construct an accurate composite solution. Both the numerical and analytical solutions are simpler and more easily obtained than the solution of the original problem, and the overall solution procedure is accurate and computationally efficient. The ANM approach has the ability to provide a high degree of spatial resolution in local areas without great computational burden.

ANM finds accurate solutions to physical problems having small scales or rapid variations that challenge the accuracy of the numerical method. In ANM, an artificial smoothing of the physical problem is introduced. The smoothing length scale must be smaller than the large length scales in the problem, but larger than the scale of numerical discretization. Because the smoothing length scale is larger than the scale associated with the numerical discretization, the numerical solution of the smoothed problem is very accurate. However, the actual problem has a physical length scale smaller than the numerical discretization. The local region associated with the small scale is solved separately (usually analytically, but sometimes numerically) as a high-resolution local problem that captures the small scales and rapid variations. This local problem, because of its idealizations, becomes invalid with increasing distance from the local region of rapid change.

The numerical problem and the local problem are combined by asymptotic matching to form a composite solution. ANM utilizes a matching procedure similar to the method of matched asymptotic expansions (MAE), but otherwise it differs from MAE in several important ways. The ANM approach requires a matching solution

that is similar to the local problem but is solved with the smoothing imposed. The smoothing length scale is the largest scale associated with the local region, but is still small compared to global scales. This scale separation allows these local solutions (high resolution and matching) to be solved with simplified geometry. The composite solution is then given by the low-resolution global numerical solution plus the high-resolution local solution minus the matching solution. In the local region, the matching solution subtracts away the local error associated with the smoothed numerical solution, leaving the local solution. Far from the local region, the local solution and the matching solution cancel, because they become identical beyond the smoothed region. For the method to work well, the degree of smoothing must be chosen to achieve a mathematical overlap so that the transition zone between the local and numerical solutions is accurate.

III.   Problem Formulation

A.   Governing Equations

In general, the governing equation of linear, compressible, unsteady potential flow can be written[15, 16]

$$\left(1 - \frac{U_\infty^2}{a_\infty^2}\right)\frac{\partial^2 \varphi}{\partial x^2} + \frac{\partial^2 \varphi}{\partial y^2} + \frac{\partial^2 \varphi}{\partial z^2} - 2\frac{U_\infty}{a_\infty^2}\frac{\partial^2 \varphi}{\partial x \partial t} - \frac{1}{a_\infty^2}\frac{\partial^2 \varphi}{\partial t^2} = 0 \quad (1)$$

The equation is derived by assuming small disturbances about a uniform freestream of compressible fluid of velocity U_∞ and is referred to as the convective wave equation. Further details of the derivation can be found in the cited references.[14, 15, 17] Note, however, if $U_\infty = 0$ then Eq. (1) becomes the simple wave equation, which governs linear acoustics, and if $a_\infty \rightarrow \infty$ it becomes Laplace's equation, which governs incompressible aerodynamics.

When solving boundary value problems associated with Eq. (1), the solutions appearing in relation to Green's theorem[18, 19] and Kirchhoff's formula[17, 20] are of special significance.[15, 17] These solutions are primarily extensions of the familiar concepts of sources and doublets from the theory of incompressible aerodynamics and acoustics.[21, 22]

Kirchhoff's formula, the analytical statement of Huygen's principal for sound waves,[23] may be expressed as a surface integration giving the potential at any point in the field in terms of a surface distribution of sources and doublets. Kirchhoff's formula for a fixed surface S and a subsonic uniformly moving medium can be expressed as

$$\varphi(x, y, z) = \frac{1}{4\pi}\int_S \left\{ \left[\frac{\partial}{\partial n}\varphi\left(t - \frac{D}{a_\infty}\right) \middle/ R \right] \right.$$
$$\left. - \frac{\partial}{\partial n}\left[\varphi\left(t - \frac{D}{a_\infty}\right) \middle/ R \right] \right\} dS \qquad (2)$$

where the quantities R and D given by

$$R = \sqrt{(x - \xi)^2 + \beta^2[(y - \eta)^2 + (z - \zeta)^2]}$$
$$D = (1/\beta^2)[-M(x - \xi) + R] \qquad \beta = \sqrt{1 - M^2}$$

are designated the amplitude radius and phase radius, respectively.[17]

If we recognize that Eq. (2) can be written in terms of the jump in potential $\Delta\varphi$ on the boundary S,[18, 19, 24] the first term in the Eq. (2) becomes a source of strength $\partial\Delta\varphi/\partial n$ in uniform rectilinear motion with the reference coordinate system attached to the source. Similarly, the second term becomes a uniformly translating doublet of strength $\Delta\varphi$. In both cases, the source and doublet strength are arbitrary functions of time. Assuming a harmonic time dependence, and denoting the source and doublet strengths, respectively, as σ and μ, Eq. (2) becomes

$$\bar{\varphi}(x, y, z) = \frac{1}{4\pi}\int_S \left\{ \sigma\frac{e^{-i\omega\tau}}{R} - \mu\frac{\partial}{\partial n}\frac{e^{-i\omega\tau}}{R} \right\} dS \qquad (3)$$

where $\varphi = \bar{\varphi}e^{i\omega t}$ and $\tau = D/a_\infty$.

Evaluating Eq. (3) on the surface S produces an integral equation for $\bar{\varphi}$. If $U_\infty = 0$ then Eq. (3) becomes a solution to the simple wave equation, and if $a_\infty \rightarrow \infty$ it becomes a solution to Laplace's equation. Therefore, when considering an arbitrary lifting surface in an

infinite medium, we take S to be the surface of the body and the wake. The boundary conditions can be specified as a Neumann problem, a Dirichlet problem, or some combination of the two. Specifically for the work in this paper, a Neumann boundary condition was assumed. This simply requires taking the normal derivative of Eq. (3), thereby recasting the problem in terms of the known normal wash specified on the surface S, which includes the body surface and the wake, and the unknowns σ and μ.

In general, a boundary element or panel method is produced when the surface is discretely approximated by a contiguous set of small elements or panels. Typically, the panels are quadrilaterals. The singularity strength can be constant over the panel or vary in some higher-order fashion. In the case of steady aerodynamics, a constant strength doublet panel representation is equivalent to a vortex lattice. Using the discrete representation, the integral equation is evaluated at collocation points. Thus, a set of algebraic equations for the singularity strengths on the panels is obtained:

$$\left[\frac{\partial \hat{\varphi}}{\partial n}\right]_k = \frac{1}{4\pi}\sum A_{kj}\sigma_j + \frac{1}{4\pi}\sum B_{kj}\mu_j + \frac{1}{4\pi}\sum D_{kj}\mu_j \quad (4)$$

The influence coefficients depend only on the geometry, not the boundary conditions and, therefore, are fixed for rigid body motion and a prescribed wake geometry.

B. Smoothed Doublets

The ANM smoothed global solution, as shown in Fig. 1, is constructed by an overlapping distribution of smoothed doublet solutions to Eq. 1. A smoothed doublet is analogous to the familiar singular doublet solution for compressible unsteady flow, except there is a spatial distribution of doublet strength density.[6–9,14] Smoothed doublets (shown in Fig. 2), are nonsingular everywhere, and away

Fig. 1 ANM smoothed global solution constructed from an overlapping distribution of smoothed aerodynamic doublets.

a) Discrete and smoothed doublets

b) ANM high-resolution local solutions

c) ANM low-resolution matching solutions

Fig. 2 Building blocks of the ANM solution.

from the distribution region, they asymptotically approach the same behavior as an equivalent singular doublet with the same aggregate strength. Note that Fig. 2 is for illustration purposes only and, in fact, the smoothed doublet exhibits a far more complex shape in terms of doublet strength and velocity distribution than that shown. Smoothed doublets can be constructed from singular doublets by a simple transformation of the radial variable,

$$R \longrightarrow R_s = \sqrt{(x-\xi)^2 + \beta^2[(y-\eta)^2 + (z-\zeta)^2 + r_c^2]}$$

or

$$R_s^2 = R^2 + \beta^2 r_c^2$$

where r_c is the additional smoothing length scale, the source origin is located at (ξ, η, ζ), and a field point is denoted (x, y, z). This construction can be done so that a velocity potential exists.[6,7,14] Overlapping discrete smoothed doublets have been shown to approximate a continuous distribution accurately.[6,8,9,14] In three dimensions, the potential for a smoothed source in rectilinear motion with harmonic source strength, therefore, can be written

$$\bar{\varphi}_{\text{source}_{\text{smooth}}} = -(\sigma/4\pi R_s)e^{-i\omega\tau_s} \quad (5)$$

where the time factor is suppressed and τ_s is defined as

$$\tau_s = (D_s/a_\infty) = (1/a_\infty\beta^2)[-M(x-\xi) + R_s]$$

The associated velocity and pressure fields can be found directly by differentiation. Distributing overlapping discrete smoothed doublets over an aerodynamic surface and associated wake is an efficient way to calculate a low-resolution smoothed global solution. This global solution, however, must be corrected by the addition of local solutions to recover the correct high-resolution answer to the original problem.

Equation (5) is a smooth function and no longer singular. There is a smooth spatial distribution of source strength concentrated about the origin of a smoothed doublet. As a result, the potential, velocity, or pressure all approach a constant value as $R \longrightarrow 0$ because $R_s \longrightarrow \beta r_c$. Note, however, as R gets large, namely, $R \gg r_c$, that these values asymptotically tend quickly toward the potential value without the smoothing imposed. In the limit when $r_c \longrightarrow 0$, the nonsmoothed potential, velocity, and pressure are recovered. The smoothed functions can be formally interpreted in a mathematical sense as convolution integrals of the nonsmooth singular results with a suitable smoothing kernel function.[25] Note that the radial smoothing used in the present work is fully self-consistent, and, therefore, two dimensional results can be simply obtained in closed form by direct integration of the three-dimensional results.

The smoothing operation takes a discrete singularity, a doublet in this case, and replaces it with a continuous distribution having the same net strength and the same far-field behavior. As a result, the region over which the singularity is distributed is no longer divergence free, although it is irrotational. The governing equation is then a inhomogeneous form of the convective wave equation [Eq. (1)] with a distributed source/sink distribution on the right-hand side. Because a doublet was smoothed to make this distribution, the distributed terms look like a source distribution above the axis and a sink distribution below. However, this distribution can also be interpreted as a spatial distribution of doublets.

When the ANM solution procedure separates the problem into local and global parts, as illustrated in Fig. 3, the global solution and the local matching solution are not divergence free and do not satisfy the homogeneous convective wave equation, but rather the inhomogeneous form of the equation. When the composite solution is constructed for this linear problem, the distributed source/sink effects from the global and matching solutions cancel (after all, their equal and opposite nature was the basis for decomposing the solution in Fig. 3), and the composite solution does satisfy the homogeneous equation.

This part of the solution procedure, which involves a decomposition by adding and subtracting smoothed singularities, is actually one of the keys to how the method works. Understanding the role of smoothing is a subtle point, especially since the smoothing cancels out in the final answer. This process is one of the real innovations of the ANM method.
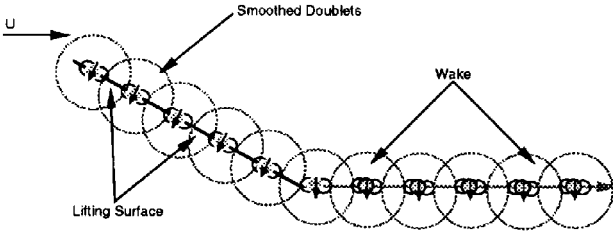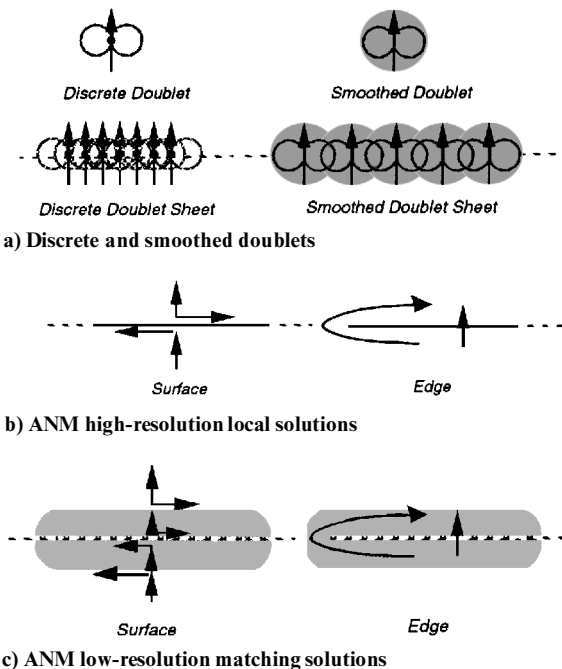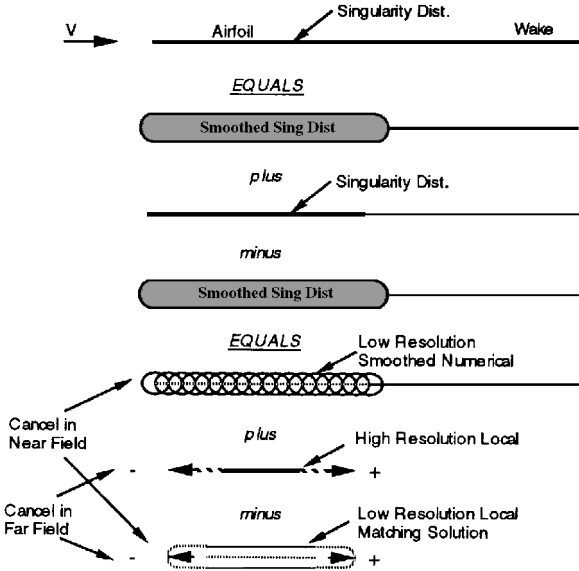
Fig. 3 Schematic representation of the ANM solution methodology for aerodynamics.

C. ANM Aeroacoustics

A distribution of smoothed doublets, as given by Eq. (5), is added and subtracted to Eq. (3) (without the source term), with no net change in the equation, giving

$$
\bar{\varphi}(x, y, z) = \left[\frac{1}{4\pi} \int \int_{S_b + S_w} \left\{ \mu \left[\frac{\partial}{\partial n} \left(\frac{e^{-i\omega\tau_s}}{R_s} \right) \right] \right\} dS \right.
$$

$$
+ \left(\frac{1}{4\pi} \int \int_{S_b + S_w} \left\{ \mu \left[\frac{\partial}{\partial n} \left(\frac{e^{-i\omega\tau}}{R} \right) \right] \right\} dS
$$

$$
\left. - \frac{1}{4\pi} \int \int_{S_b + S_w} \left\{ \mu \left[\frac{\partial}{\partial n} \left(\frac{e^{-i\omega\tau_s}}{R_s} \right) \right] \right\} dS \right) \right] \tag{6}
$$

where b denotes the body surface and w denotes the wake surface. Combining the two integrals in the second term on the right-hand side and taking the normal derivative gives

$$
\bar{v}_n(x, y, z) = \boldsymbol{n} \cdot \left(\frac{1}{4\pi} \int \int_{S_b + S_w} \left\{ \mu \nabla \left[\frac{\partial}{\partial n} \left(\frac{e^{-i\omega\tau_s}}{R_s} \right) \right] \right\} dS \right.
$$

$$
\left. + \frac{1}{4\pi} \int \int_{S_b + S_w} \left\{ \mu \nabla \left[\frac{\partial}{\partial n} \left(\frac{e^{-i\omega\tau}}{R} \right) - \frac{\partial}{\partial n} \left(\frac{e^{-i\omega\tau_s}}{R_s} \right) \right] \right\} dS \right) \tag{7}
$$

where $\bar{v}_n$ denotes the velocity normal to the surface, following the notation convention $v_n = \bar{v}_n e^{i\omega t}$. Notice that the integrand in the second term on the right-hand side of Eq. (7) becomes negligible when $r \gg r_c$, because $R_s \longrightarrow r$, $\tau_s \longrightarrow \tau$, and the value of the smooth doublet kernel function approaches that of the singular kernel function, and they asymptotically cancel each other. The contribution of this integral becomes significant only when $r = \mathcal{O}(r_c)$.

On the surface $S_b + S_w$ where $\bar{v}_n$ is specified, there is a small region S_{r_c} about $p = (x, y, z)$ where $r = \mathcal{O}(r_c)$. Most of the contribution to the integral comes from this region S_{r_c} immediately about p. Therefore, the bounds of integration can be modified such that the integration is done on any surface S_{mod} that contains S_{r_c}, without changing the final result.

Because of the local nature of the integral over S_{mod}, a series expansion about $p = (x, y, z)$ can be written for the doublet strength density

$$
\mu(\boldsymbol{p} + \Delta \boldsymbol{r}) = \mathcal{F}(\Delta \boldsymbol{r}) \sum_{k=0}^{\infty} \frac{1}{k!} (\Delta \boldsymbol{r} \cdot \nabla)^k \mu(\boldsymbol{p}) \tag{8}
$$

where $\Delta \boldsymbol{r}$ is the vector change in position on the surface, $\boldsymbol{p}$ is the vector location of p, and $\mathcal{F}(\Delta \boldsymbol{r})$ is a weighting function having to do with the local solution, discussed in the next section. Essentially, $\mathcal{F}(\Delta \boldsymbol{r})$ is included because the doublet strength density may be nonanalytic approaching the edges of the lifting surface. Only the first few terms in the series are necessary; however, at this point the entire series is retained for completeness. Substituting the series expression into Eq. (7), and changing the bounds of integration on the second integral from $S_b + S_w$ to S_{mod} gives

$$
\bar{v}_n(x, y, z) = \boldsymbol{n} \cdot \left(\frac{1}{4\pi} \int \int_{S_b + S_w} \left\{ \mu \nabla \left[\frac{\partial}{\partial n} \left(\frac{e^{-i\omega\tau_s}}{R_s} \right) \right] \right\} dS \right.
$$

$$
+ \frac{1}{4\pi} \int \int_{S_{\text{mod}}} \left\{ \mathcal{F} \sum_{k=0}^{\infty} \frac{1}{k!} (\Delta \boldsymbol{r} \cdot \nabla)^k \mu(\boldsymbol{p}) \nabla \left[\frac{\partial}{\partial n} \left(\frac{e^{-i\omega\tau}}{R} \right) \right. \right.
$$

$$
\left. \left. \left. - \frac{\partial}{\partial n} \left(\frac{e^{-i\omega\tau_s}}{R_s} \right) \right] \right\} dS \right) \tag{9}
$$

This can then be rewritten as

$$
\bar{v}_n(x, y, z) = \boldsymbol{n} \cdot \left[\frac{1}{4\pi} \int \int_{S_b + S_w} \left\{ \mu \nabla \left[\frac{\partial}{\partial n} \left(\frac{e^{-i\omega\tau_s}}{R_s} \right) \right] \right\} dS \right.
$$

$$
+ \sum_{k=0}^{\infty} \left(\bar{\varphi}_k^{\text{local}}(p) - \mathcal{F} \frac{1}{4\pi} \int \int_{S_{\text{mod}}} \left\{ \frac{1}{k!} (\Delta \boldsymbol{r} \cdot \nabla)^k \right. \right.
$$

$$
\left. \left. \left. \times \mu(p) \nabla \left[\frac{\partial}{\partial n} \left(\frac{e^{-i\omega\tau_s}}{R_s} \right) \right] \right\} dS \right) \right] \tag{10}
$$

where

$$
\bar{\varphi}_k^{\text{local}}(p) = \mathcal{F} \frac{1}{4\pi} \int \int_{S_{\text{mod}}} \left\{ \frac{1}{k!} (\Delta \boldsymbol{r} \cdot \nabla)^k \mu(\boldsymbol{p}) \nabla \left[\frac{\partial}{\partial n} \left(\frac{e^{-i\omega\tau}}{R} \right) \right] \right\} dS \tag{11}
$$

$\bar{\varphi}_k^{\text{local}}$ is the local potential, and in Eq. (11) it is written in terms of an integral over the surface S_{mod}. This integral represents a family of simple flow solutions to the convective wave equation, which can be found by perturbation methods and separation of variables. As such, the explicit integration of Eq. (11) is not required. Equation (10) is the fundamental integral equation of the ANM boundary element method. In two dimensions Eq. (10) becomes

$$
\bar{v}_n^{2D}(x, z) = -\boldsymbol{n} \cdot \left[\frac{i}{4} \int_{\Gamma_b + \Gamma_w} \left(\mu_{2D} \nabla \left\{ \frac{\partial}{\partial n} \left[H_0^2(k\hat{R}_s) \right] \right\} \right) dS \right.
$$

$$
+ \sum_{k=0}^{\infty} \frac{\mu_{2D}^{(k)}(p)}{k!} \left(\bar{\varphi}_k^{\text{local}}(p) - \frac{i}{4} \mathcal{F} \int_{\Gamma_{\text{mod}}} (x - p)^k \right.
$$

$$
\left. \left. \times \nabla \left\{ \frac{\partial}{\partial n} \left[H_0^2(k\hat{R}_s) \right] \right\} dS \right) \right] \tag{12}
$$

where

$$
\bar{\varphi}_k^{\text{local}}(p) = \frac{i}{4} \mathcal{F} \int_{\Gamma_{\text{mod}}} (x - p)^k \nabla \frac{\partial}{\partial n} \left[H_0^2(k\hat{R}) \right] dS \tag{13}
$$

and

$$
\hat{R} = \sqrt{(x - \xi)^2 + \beta^2 (z - \zeta)^2} \longrightarrow \hat{R}_s
$$

$$
= \sqrt{(x - \xi)^2 + \beta^2 [(z - \zeta)^2 + r_c^2]}
$$

Again $\bar{\phi}_k^{\text{local}}$ represents simple flow solutions to the convective wave equation, the caret notation denotes two dimensions, Γ_{mod} is a contour that contains Γ_{r_c}, and the series expansion is taken about $p = (x, z)$.

Note that, if the point p is not on the surface $S_B + S_w$, Eqs. (10) and (12) are integral representations of the normal velocity field, in terms of the normal velocity field on the surface $S_b + S_w$. If the point p is on S_b, Eqs. (10) and (12) become inhomogeneous Fredholm integral equations of the first kind, relating the known normal velocity $\bar{v}_n$ to the unknown values of μ on S_b, where the values on S_w can be explicitly determined from the values on S_b. At this point, the advantage of using Eqs. (10) and (12) may not be clear; however, it will be shown that due to their smooth nature these equations are advantageous for numerical implementation.

Examining the terms in Eq. (10) in greater detail reveals the relationship between the original problem [Eq. (3)] and the problem cast in terms of ANM. The ANM methodology breaks the problem up into global and local constituent parts. It will be shown that the first term on the right-hand side of the equation embodies smoothed global effects, ultimately treated numerically, whereas the second term is a local correction that can be found analytically.

The relationship between the original problem and its ANM constituent problems is shown in Fig. 3, which depicts the ANM decomposition of the original linear problem. As a first step, equivalent smoothed singularity distributions are added to and subtracted from the original problem. Because these smoothed distributions exactly cancel, the net result is unchanged. However, the singularity distributions can also be regrouped. The first smoothed singularity distribution can be viewed as the low-resolution smoothed global problem and can be represented by discrete overlapping smoothed doublets as shown in Fig. 3 (also see Fig. 1). The second (original) distribution and the third (smoothed) distribution can be combined. When this is done, these two distributions always cancel asymptotically at points away from the point of evaluation, because they have the same far-field limiting behavior. Thus, only the local behavior of these distributions ultimately matters. For convenience, they can be evaluated as if they are part of an infinite sheet (or a semi-infinite sheet if near an edge). Using a Taylor series expansion of the singularity strength distribution in this local region, it can be shown that these local solutions can be expressed in terms of simple flowfields obtained from the governing equation by separation of variables.[6–9,14]

D. ANM Local Correction

The ANM local correction[6–9, 14] is the difference between a high-resolution local solution based on singular doublets and a corresponding smoothed local solution, called the matching solution, based on smoothed doublets. Figure 2 shows sketches of local solutions for surfaces and near edges. The difference between these solutions cancels far away, because they have the same limiting behavior in the far field. Therefore, the far-field shape and behavior is unimportant, allowing very simple solution forms to be used. Appropriate high-resolution local solutions on surfaces and near edges can be found by separation of variables, perturbation methods, or by direct integration over singular doublet distributions of infinite or semi-infinite extent. Matching solutions can found by integration over corresponding smoothed doublet distributions, or by a special variable separation technique combined with an equivalent singularity displacement method called the split sheet analogy.[6] In model problems solved to date, the variable separation methods have been easier and more physically insightful.

The local correction is based on the second term on the right-hand side of Eq. (10), which represents the difference between a distribution of conventional doublets and smoothed doublets. The difference between these distributions cancels far away; therefore, the far-field shape and behavior is unimportant, allowing for simplification in the evaluation of the integral. The domain of integration only needs to be geometrically correct immediately about p. In particular, when considering a flat surface, for convenience, the bounds of integration can be taken to infinity. The integration is done on an infinite flat surface (a contour in two dimensions) with p located at the origin, given by

$$\mathcal{L} = \boldsymbol{n} \cdot \left\{ \frac{1}{4\pi} \int_{-\infty}^{\infty} \int_{-\infty}^{\infty} \mathcal{F} \sum_{k}^{\infty} \frac{1}{k!} (\Delta \boldsymbol{r} \cdot \nabla)^k \right.$$
$$\left. \times \mu(p) \nabla \left[\frac{\partial}{\partial n} \left(\frac{e^{-i\omega\tau}}{R} \right) - \frac{\partial}{\partial n} \left(\frac{e^{-i\omega\tau}}{R_s} \right) \right] dS \right\} \tag{14}$$

where $\mathcal{L}_w$ denotes the net local correction. Any effects from the far field will cancel, leaving only the local difference between the smoothed and conventional distributions. Therefore, in practice, only the first few terms in the series need to be retained. Special consideration is made for edges, due to the additional length scale that measures from the tip of the edge to p. A point p is determined to be close to the edge if it is a distance of $O(r_c)$ from the edge. In this case, the integration is taken over semi-infinite bounds along the edge coordinate direction, starting at the edge, where p is located a distance l inboard of the edge

$$\mathcal{L}_w^{\text{edge}} = \boldsymbol{n} \cdot \left\{ \frac{1}{4\pi} \int_{0}^{\infty} \int_{-\infty}^{\infty} \mathcal{F} \sum_{k}^{\infty} \frac{1}{k!} (\Delta \boldsymbol{r} \cdot \nabla)^k \right.$$
$$\left. \times \mu(p) \nabla \left[\frac{\partial}{\partial n} \left(\frac{e^{-i\omega\tau}}{R} \right) - \frac{\partial}{\partial n} \left(\frac{e^{-i\omega\tau_s}}{R_s} \right) \right] dS \right\} \tag{15}$$

The contribution of the distribution of conventional doublets in Eqs. (14) and (15), the first term in the square brackets, is called the high-resolution local solution. It contains the details of the local flow structure, including the local gradients. Looking specifically at this part of the integral, it can easily be shown that the high-resolution local solution consists of exact solutions to the convective wave equation on an infinite or semi-infinite domain. This is because it consists of integral distributions of freespace Green's functions with varying strength distributions given by the terms in the series, which explicitly satisfy the boundary conditions. As such, by considering the terms in the Taylor series of the doublet strength distribution in Eqs. (14) and (15), the flowfield about a control point can be deduced in terms of simple exact solutions to the convective wave equation on an infinite domain.

Therefore, using the Taylor series as a guide, perturbation solutions to the convective wave equation can be found that match the power of each term in the series and represent an approximation to the integrated singular Green's function distributions given in Eqs. (14) and (15). As noted earlier, the series can be truncated at any desired accuracy; however, depending on S_{mod}, care must be taken to assure that the resulting integrals are uniformly convergent. In the present implementation, the series was truncated after the quadratic terms.

The contribution of the distribution of smoothed doublets in Eqs. (14) and (15), the second term in the square brackets, is called the matching solution. It cancels the global solution locally, and the local high-resolution solution globally, thereby asymptotically matching the global solution to the local high-resolution solution. The matching solution is precisely a smoothed version of the high-resolution local solution.

The smoothing, as shown in Fig. 2, can be done by any suitable means; however, a technique called the split-sheet analogy is effective. This approach is based on the observation that the smoothing process is similar to viewing a singular solution at an offset location. In particular, consider the smoothed doublet velocity field by taking the appropriate derivative of Eq. (5). When viewed in the $z = 0$ plane, which is the surface on which the downwash is evaluated, this expression can be shown to be the same as that for a discrete source and sink displaced a distance r_c above and below the $z = 0$ plane, respectively, provided the doublet strength and source strength are related as $\mu = 2 r_c \sigma$. It follows that a sheet of smoothed doublets on $z = 0$ can be replaced by corresponding sheets of discrete sources and sinks, offset above and below $z = 0$ by distance r_c. For the calculation of downwash, smoothing a doublet sheet is

equivalent to splitting the doublet sheet into its constituent source and sink sheets displaced an appropriate amount. This approach leads to a simple way to construct smoothed local solutions using separation of variables. Because the local solutions can be interpreted basic flows obtained by separation of variables, the smoothed local solutions used for matching can also be obtained in a similar manner. However, these flows must be associated with source/sink surfaces, rather than doublet surfaces. Furthermore, the downwash associated with these surfaces must be evaluated at positions offset above and below the surfaces a distance r_c. This approach, which has been verified by other means (direct integration of the kernel function), has been found to be particularly straightforward and insightful.

The net local correction is the difference between the high-resolution local solution and the matching solution, the terms in the square brackets of Eqs. (14) and (15). For a flat surface with coordinates (x, y), the net local correction $\mathcal{L}_w$ at the point (x_1, y_1), in terms of upwash is given by

$$\mathcal{L}_w = \boldsymbol{n} \cdot \left(\frac{1}{4\pi} \int_{-\infty}^{\infty} \int_{-\infty}^{\infty} \left\{ \mu(x_1, y_1) + (x - x_1)\frac{\partial \mu}{\partial x} + (y - y_1)\frac{\partial \mu}{\partial y} \right. \right.$$

$$+ \frac{1}{2!}\left[(x - x_1)^2 \frac{\partial^2 \mu}{\partial x^2} + 2(x - x_1)(y - y_1)\frac{\partial^2 \mu}{\partial x \partial y} \right.$$

$$\left. \left. + (y - y_1)^2 \frac{\partial^2 \mu}{\partial y^2} \right] \right\} \nabla \left[\frac{\partial}{\partial n}\left(\frac{1}{R} \right) - \frac{\partial}{\partial n}\left(\frac{1}{R_s} \right) \right] dS \right)$$

$$\approx -\frac{\mu}{2r_c}\left(1 - \frac{1}{2}(kr_c)^2 + \cdots \right) - \frac{i}{2}\frac{\partial \mu}{\partial x} M[(kr_c) + \cdots]$$

$$+ \left(\frac{\partial^2 \mu}{\partial x^2} + \frac{\partial^2 \mu}{\partial y^2} \right)\left(\frac{\beta^2 r_c}{4} + \cdots \right) \tag{16}$$

where the truncated Taylor series has been substituted into Eq. (14) and $\mathcal{F}$ is taken as unity. The expansions are truncated to $\mathcal{O}[(kr_c)^3]$.

It is documented in the literature[26,27] that for two-dimensional subsonic flow about edges there is a $\frac{1}{2}$-power singularity in the tangential velocity component just inboard of an edge. Therefore, at an edge in two dimensions or sufficiently close to an edge in three dimensions, the doublet strength distribution can expected to be expanded in powers of $\frac{1}{2}$:

$$\mu_{\text{edge}}(x) = c_0 x^{\frac{1}{2}} + c_1 x^{\frac{3}{2}} + \mathcal{O}\left(x^{\frac{5}{2}} \right) \tag{17}$$

where c_0 and c_1 are arbitrary constants.

In three dimensions, Eq. (17) can be thought of as the leading order term in an asymptotic expansion, because very close to an edge, the two-dimensional terms dominate the three-dimensional terms in the solution. This can be demonstrated with a simple perturbation expansion about the edge. Trouble could possibly arise at the wing tip corners, where two edges are present. Here, however, the flowfield can be modeled with conical flow solutions.[26,28] Numerical experimentation has shown that the conical flow solutions are not required for sufficient accuracy. If, however, higher accuracy is needed, higher-order wing tip corner solutions can be constructed from conical flow solutions.

Therefore, the weighting function $\mathcal{F}$ in Eq. (8) should be (Δr) for the edge panels (unity elsewhere), and the expansion is taken about the edge rather than about p. As mentioned earlier, this is because the doublet strength distribution becomes nonanalytic at the edge. At any point l on the surface near the edge, c_0 and c_1 can be determined in terms of the derivative of Eq. (17), ignoring terms of $\mathcal{O}(x^{3/2})$, such that

$$c_0 = \frac{3}{2}\frac{\mu_{\text{edge}}(l)}{\bar{l}} - \bar{l}\frac{d}{dx}[\mu_{\text{edge}}(x)]_{x=l}$$

$$c_1 = \frac{1}{\bar{l}}\frac{d}{dx}[\mu_{\text{edge}}(x)]_{x=l} - \frac{1}{2}\frac{\mu_{\text{edge}}(l)}{l^{\frac{3}{2}}} \tag{18}$$

The series expansion of the doublet distribution for an edge [Eq. (17)] can now be written in terms of the doublet strength density and its derivative as

$$\mu_{\text{edge}}(x) = \left(\frac{3}{2}\frac{\mu_{\text{edge}}(l)}{\bar{l}} - \sqrt{\bar{l}}\frac{d}{dx}[\mu_{\text{edge}}(x)]_{x=l} \right) x^{\frac{1}{2}}$$

$$+ \left(\frac{1}{\bar{l}}\frac{d}{dx}[\mu_{\text{edge}}(x)]_{x=l} - \frac{1}{2}\frac{\mu_{\text{edge}}(l)}{l^{\frac{3}{2}}} \right) x^{\frac{3}{2}} \tag{19}$$

where x can be any coordinate direction inboard of the edge.

After substitution of Eq. (19) into Eq. (15) and evaluation [similar to Eq. (16)], the corresponding correction in terms of upwash for edges is

$$\mathcal{L}_w^{\text{edge}} = \frac{c_0}{2r_c}(r\beta)^{\frac{1}{2}}\left\{ \cos\frac{\theta}{2} + (kr)\frac{i\gamma}{2}\left(\cos\frac{\theta}{2} - \cos\frac{3\theta}{2} \right) \right.$$

$$+ (kr)^2\left[\frac{\gamma^2}{24}\left(4\cos\frac{\theta}{2} - 3\cos\frac{3\theta}{2} \right) - \left(\frac{\gamma^2}{60} + \frac{1}{30} \right) \right.$$

$$\times \left(5\cos\frac{\theta}{2} - 2\cos\frac{5\theta}{2} \right) + \left. \left. \left(\frac{\gamma^2}{120} + \frac{1}{10} \right)\cos\frac{5\theta}{2} \right] \right\}$$

$$+ \frac{c_1}{2r_c}(r\beta)^{\frac{3}{2}}\left\{ \cos\frac{3\theta}{2} + (kr)\frac{i\gamma}{2}\left(\cos\frac{\theta}{2} - \cos\frac{5\theta}{2} \right) \right.$$

$$+ (kr)^2\left[\frac{-\gamma^2}{40}\left(5\cos\frac{\theta}{2} - 4\cos\frac{3\theta}{2} \right) + \left(\frac{\gamma^2}{140} - \frac{1}{70} \right) \right.$$

$$\times \left. \left. \left(7\cos\frac{3\theta}{2} - 2\cos\frac{7\theta}{2} \right) + \left(\frac{1}{14} - \frac{3\gamma^2}{280} \right)\cos\frac{7\theta}{2} \right] \right\} + \cdots \tag{20}$$

the next term in the expansion is $\mathcal{O}(r)^{5/2}]$, where

$$r = \sqrt{(x/\beta)^2 + r_c^2} \qquad \theta = \arctan(\beta r_c / x)$$

$$\gamma = M/\beta = M/\sqrt{1 - M^2} \qquad \beta = \sqrt{1 - M^2}$$

The preceding integrations were done using the split-sheet analogy. Therefore, the calculation of each integral involved Taylor series expansions of the nondimensional grouping (kr_c) or (kr). It follows that each solution is valid for $(kr_c \ll 1)$ or $(kr \ll 1)$, unless additional higher-order terms are kept in the expansions. Numerical practice has shown, however, that this limitation is rather weak. Cases even only loosely adhering to the limit $(kr_c \ll 1)$ or $(kr \ll 1)$, namely, $(kr_c < 1)$ or $(kr < 1)$, performed well in comparison with available closed-form results.

E. Composite ANM Solution

Following the development of Fig. 3, the preceding discussion, and the cited references,[6–9,14] the ANM composite solution satisfies the integral equation given by Eq. (21). The composite solution is formed from the low-resolution global solution, plus the high-resolution local solution, denoted $\mathcal{L}$ in Eq. (21), minus the low-resolution local matching solution, denoted $\mathcal{M}$ in Eq. (21). As Eq. (21) indicates, the local solutions scale with doublet strength, as does the global solution,

$$\frac{\partial \bar{\varphi}}{\partial n} = -\frac{1}{4\pi}\int_S \left\{ \mu\frac{\partial^2}{\partial n^2}\frac{e^{-j\omega \tau_s}}{R_S} \right\} dS + \mu\mathcal{L} - \mu\mathcal{M} \tag{21}$$

An interesting feature of the ANM composite solution is that all its constituent parts are functionally smooth. In fact, it is only vaguely reminiscent of a traditional panel method. The surface S of Eq. (3) is no longer discretely approximated by a contiguous set of panels, but, rather, a discrete distribution of overlapping smoothed doublets. Therefore, the idea of a surface of contiguous panels exists only with regard to the spacing between adjacent smoothed doublets.

This smoothness leads to accurate, rapidly converging numerics. In addition, the analytical aspects of the problem are well defined and well behaved. In contrast to traditional discretized calculations, there is no ambiguity as to whether local averages or point values of variables, such as pressure, are being computed on panels. ANM computes local values of variables and even handles singular behavior at edges in a formal manner that allows singularity strength to be determined. Sources of error are quantifiable, and there is a procedure for extending the method to higher-order accuracy.

IV. Numerical Results

This section presents results for ANM boundary element calculations of linear, unsteady, compressible flow about lifting flat plate airfoils in two dimensions and rectangular wings in three dimensions. Calculations include the aerodynamic loading and far-field acoustic radiation from unsteady heave or pitch and nonuniform inflow conditions. Comparison is made with classical solutions when possible.

In previous work, the ANM methodology has been applied to both steady linear aerodynamics[6] and linear acoustics.[8] In both applications, the method has been rigorously verified by comparison to classical solutions. To this end, steady compressible and incompressible aerodynamic problems have been modeled accurately. In addition, a multitude of acoustic problems have been addressed, including: fluid loading, acoustic scattering, and radiation calculations. Throughout this developmental work, the ANM boundary element method proved to be a robust and versatile methodology providing accurate results.

Two familiar problems from the theory of classical unsteady aerodynamics are the Theodorsen problem,[29] namely, a flat plate airfoil subject to harmonic unsteady heave and pitch, and the von Kármán–Sears problem[30] or that of an airfoil encountering a harmonic nonuniform inflow. Both of these problems involve unsteady incompressible flow ($k \ll 1$), for which there are readily available exact analytical solutions.

Consider the lift due to a harmonic nonuniform inflow; Fig. 4 shows both components of the complex lift as a parametric function of the reduced frequency k_r. The imaginary component of the lift is plotted along the ordinate and the real component along the abscissa. The calculation used 100 smoothed doublets along the chord, with a smoothing radius r_c of 1.5 times the doublet spacing d_s. This large number of doublets assures that the effects of the higher reduced frequencies are accurately captured. The lift is nondimensionalized by the freestream velocity U_∞ the freestream density ρ_∞ the semichord b, and the gust velocity W_g. There is excellent agreement between the ANM and the exact solution using von Kármán–Sears theory. The same results were calculated independent of control point/influence point positioning. This issue will be addressed in greater detail later. Similar calculations were done for a flat plate subject to harmonically varying heave, and the ANM results compare favorably to the exact unsteady lift calculation done using Theodorsen theory.[9]
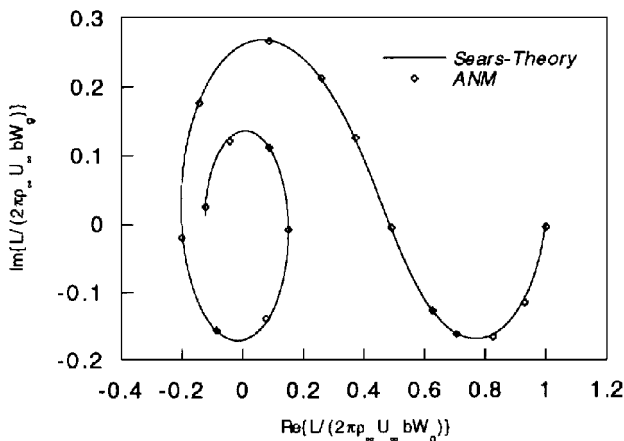
Fig. 4   Complex lift due to unsteady harmonic nonuniform inflow as a parametric function of reduced frequency.

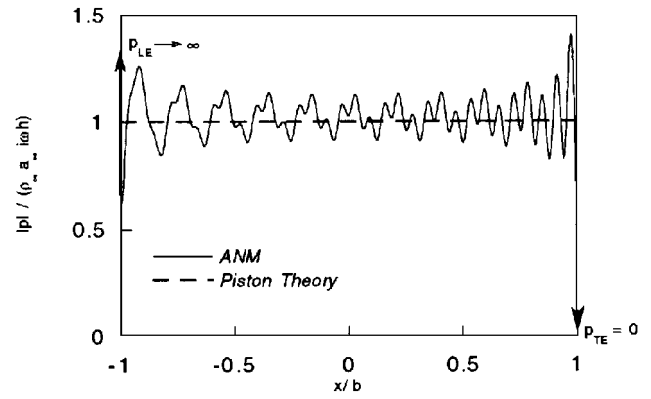**Fig. 5   Surface perturbation pressures for an oscillating flat plate airfoil: $kC = 100$, $k_r = 100$, $M = 0.5$, $r_c/d_s = 1.75$, $kb = 50$, and $\lambda/C = 2\pi/100$.**
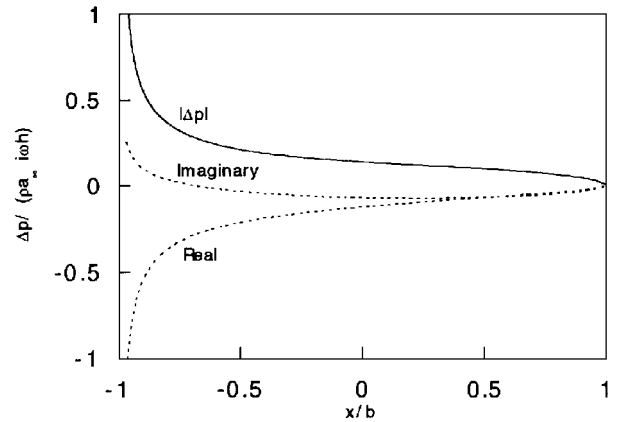
Fig. 6   Upper and lower surface pressure difference for an oscillating flat plate airfoil: $kC = 0.1$, $k_r = 0.5$, $M = 0.1$, $r_c/d_s = 1.5$, $kb = 0.05$, and $\lambda/C = 62.8$.

In Fig. 4 the ANM method accurately captures the unsteady aerodynamics across a wide range of reduced frequencies. The small discrepancies between the ANM solutions and the exact solutions are due the discrete nature of the ANM solution. In previous steady aerodynamic calculations,[6] the ANM method was found to converge with as few as 10 smoothed doublets along the chord. In fact, for unsteady calculations the number of doublets needed is slightly greater than that required by the Nyquist criterion, approximately five or six doublets per wavelength.

Next consider a flat plate airfoil at high frequency, $kC = 100$, in a mean convective freestream, $M = 0.5$. Figure 5 shows the magnitude of the pressure along the chord of the oscillating plate. The frequency of oscillation is considerably high, over 30 acoustic wavelengths along the chord relative to upstream waves. In effect, this is a compressible Theodorsen problem, a flat plate undergoing heave subject to a convective freestream. Note, however, at higher frequencies in the limit as $k \rightarrow \infty$ the results of piston theory[31] should be recovered. As shown in Fig. 5, the ANM calculation approaches the anticipated piston theory limit. Note the complex wave structure of the surface pressure distribution, clearly showing the interaction of the upstream and downstream waves. Although not shown clearly in the figure, the leading-edge singularity is present. Because of the elevated frequencies involved in the problem, 500 smoothed doublets were used to assure highest accuracy. Note, however, the calculation could have been made with fewer smoothed doublets. The smoothing radius was 1.75 times the doublet spacing, $r_c/d_s = 1.75$.

Looking at a lower frequency heave calculation, Fig. 6 shows the magnitude of the pressure difference between the upper and lower surface of the plate for $kC = 0.1$, $M = 0.1$ and $k_r = 0.5$. The calculation accurately captures the leading-edge pressure singularity, and the trailing-edge pressure fall off. Right at the trailing edge, the pressure is zero, as is expected, because the fluid just downstream of
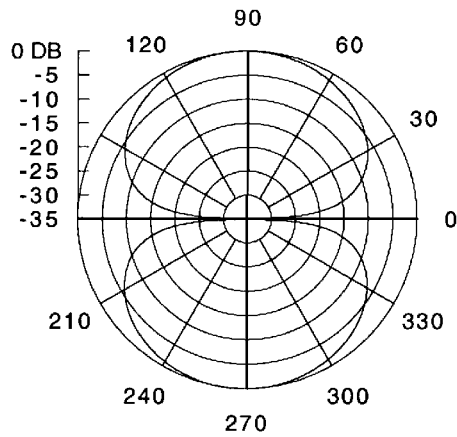
Fig. 7 Directivity pattern for an oscillating flat plate airfoil: $kC = 0.1$, $k_r = 5$, $M = 0.1$, $r_c/d_s = 1.5$, $R = 20C$, $kb = 0.05$, and $\lambda/b = 62.8$.

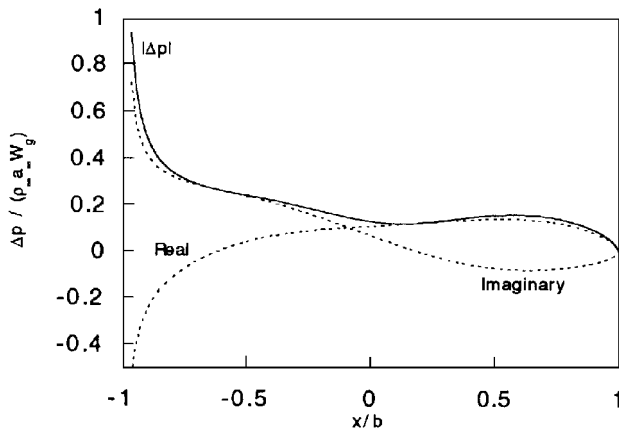**Fig. 9 Real and imaginary components of the doublet strength distribution for a flat plate airfoil subject to nonuniform sinusoidal gust: $kb = 2.5$, $k_r = 6.25$, $M = 0.4$, $r_c/d_s = 1.5$, and $\lambda_g = 1$.**

Fig. 8 Perturbation pressure difference distribution for a flat plate airfoil subject to nonuniform sinusoidal gust: $kb = 2.5$, $k_r = 6.25$, $M = 0.4$, $r_c/d_s = 1.5$, and $\lambda_g/b = 1$.

Fig. 10 Directivity pattern for a flat plate airfoil subject to nonuniform sinusoidal gust: $kb = 2.5$, $k_r = 6.25$, $M = 0.4$, $r_c/d_s = 1.5$, $\lambda_g/b = 1$, and $R = 20C$.

the trailing edge can not support a finite pressure difference across the wake. The calculation used 100 smoothed doublets; however, due to the low frequency, it could have been done with far fewer doublets. In addition, Fig. 6 shows the real and imaginary parts of the pressure difference. The pressure is dominated by the real component at lower frequencies. Figure 7 shows far-field acoustic radiation directivity pattern plotted in decibels referenced to the maximum value in the field. The pressure is taken 20 chord lengths from the center of the airfoil. The far-field acoustic radiation for this case looks like that of an isolated radiating dipole, because the plate is acoustically compact compared to upstream wavelength in the problem. Higher frequency plate oscillations were considered. As expected, more complex interactions between upstream and downstream waves were evident in the calculations, primarily due to larger convective velocities, and the fact that the plate was no longer acoustically compact. Similar trends were found in the far-field acoustic radiation directivity patterns.[9]

Next consider the response of a flat plate airfoil to a nonuniform inflow, much like a compressible von Kármán–Sears problem. Figure 8 shows the chordwise pressure difference distribution calculated for an airfoil subject to $kb = 2.5$, $k_r = 6.25$, and $M = 0.4$. The inflow upwash velocity varies sinusoidially. In this calculation, the gust wavelength is half the chord length. This calculation used 100 smoothed doublets along the chord. Just as with the heave calculations, the ANM method accurately captures the behavior at both the leading and trailing edges. Figure 8 also shows the real and imaginary components of the pressure. Similar to the Sears function results presented earlier, the pressure is nondimensionalized by the freestream density, sound speed, and gust velocity. Figure 9 shows the real and imaginary parts of the doublet strength distribution, and
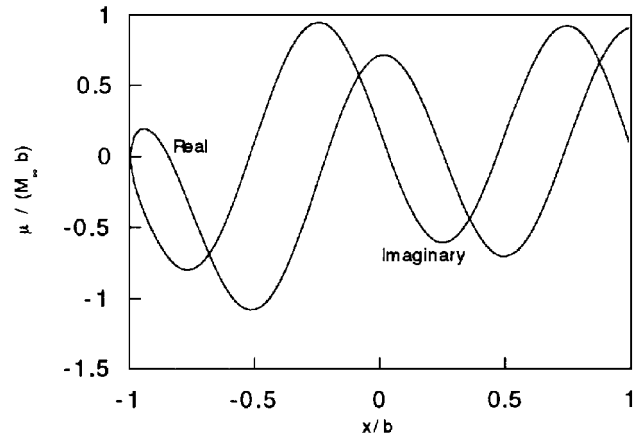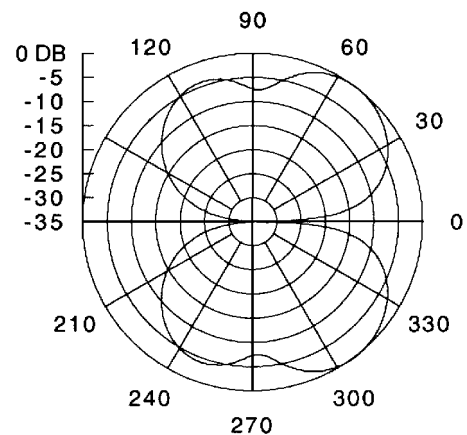
Fig. 10 shows the directivity pattern of the radiated far-field acoustic pressure. Higher gust frequencies were considered. As expected, a more detailed structure was found in the far-field calculations. This behavior was primarily due to the interference created by the higher frequency gust interaction.[9]

As discussed previously, the ANM method works in terms of doublet strength density, instead of potential, acceleration potential, or some other unknown. Therefore, the doublet strength per unit chord is calculated, and the net lift, moment, pressure distribution, and radiated acoustic field are calculated from it. Figure 9 carries all of the information that is in Fig. 8, along with the net lift and other integrated properties of the flowfield.

Looking at the effect of control-point/influence-point placement in more detail, Fig. 11 shows the chordwise pressure difference distribution, the real and imaginary components of the pressure, and doublet strength distribution for a flat plate airfoil subject to a nonuniform sinusoidal gust, with $kb = 1.6$, $k_r = 4$, and $M = 0.4$. The calculations are almost completely independent of control-point/influence-point placement. The control-point/influence-point locations are indicated as the fraction of the effective panel size, noted in the figure legend with control point location indicated first. The effective panel size is defined by the chord length divided by the total number of smoothed doublets.

Figure 12 shows the ANM calculation of net doublet strength for a flat plate oscillating in incompressible flow as a function of r_c/d_s, normalized by the linear theory result for different control-point/influence-point locations (denoted in the legend). To the left of $r_c/d_s = 1$, the three curves diverge due to discreteness errors. The global solution is no longer smooth; therefore, the ANM global/local
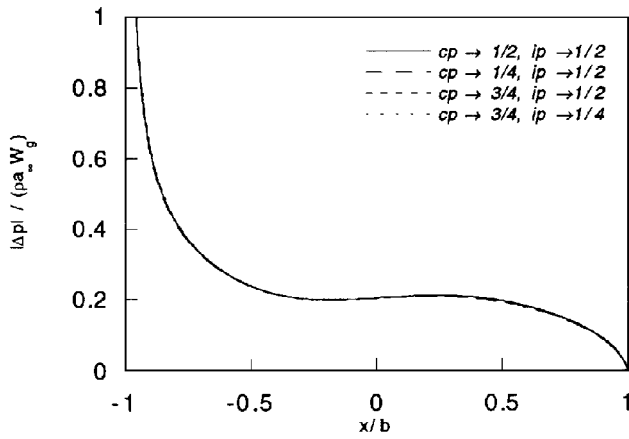
Fig. 11 Perturbation pressure difference distribution for a flat plate airfoil subject to nonuniform sinusoidal gust calculated using various control-point and influence-point positions: $kb = 1.6$, $k_r = 4$, $M = 0.4$, $r_c/d_s = 1.5$, and $\lambda_g/b = 1.57$.
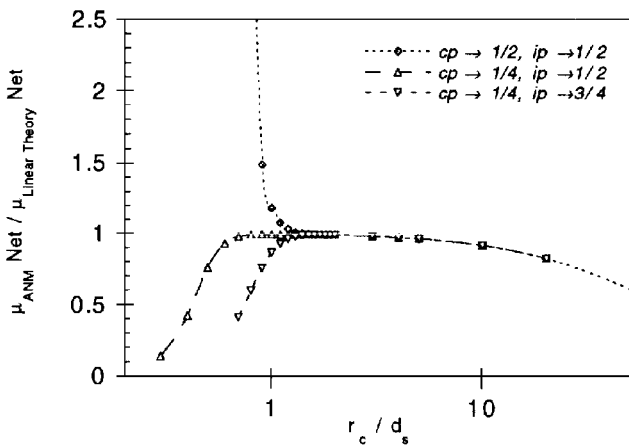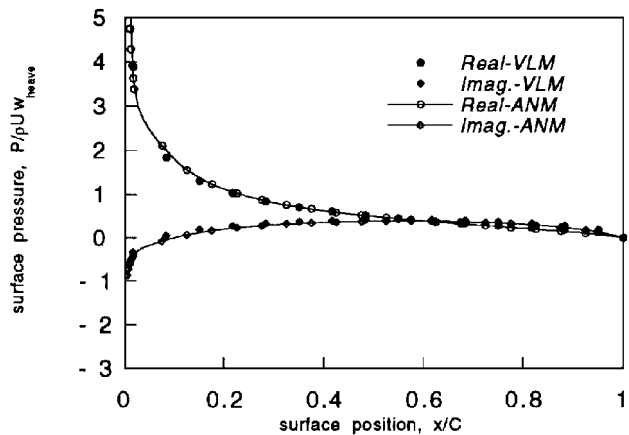

Fig. 12 ANM calculation of net doublet strength for a flat plate oscillating in incompressible flow as a function of r_c/d_s, normalized by the linear theory result for different control-point/influence-point locations.

Fig. 13 Surface perturbation pressures for an heaving rectangular wing (aspect ratio 3) in three dimensions: $k_r = 0.5$ and $r_c/d_s = 1.8$.

solution match is no longer valid. To the far right, the ANM solution loses resolution when compared to the linear theory calculation, because the global and local solutions are too smoothed. Again the ANM global/local solution match is no longer valid, thereby resulting in a loss of detailed resolution. The most important feature of Fig. 12 is relatively large solution overlap region where the ANM solution is independent of the smoothing parameter.

Considering now calculations in three dimensions, Fig. 13 shows an unsteady surface pressure calculation chordwise at the midspan
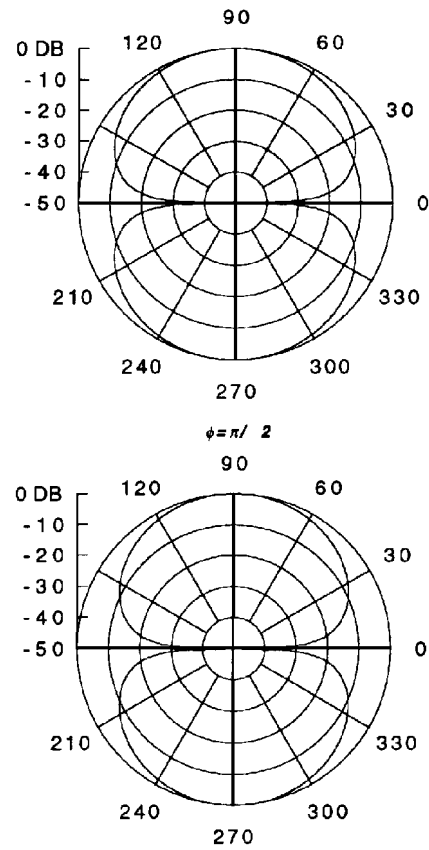

Fig. 14 Directivity pattern for a rectangular wing (aspect ratio 3) subject to harmonic heave: $kC = 1$, $k_r = 5$, $M = 0.1$, $r_c/d_s = 1.8$, $\phi = 0$, and $R = 20C$.

for a rectangular wing of aspect ratio 3 subject to harmonically varying heave, $k_r = 0.5$, in incompressible flow. The calculation was done using the ANM methodology and also with an unsteady vortex lattice formulation. The two methods compare favorably. The calculation used a grid of 60×20 smoothed doublets, with a smoothing radius r_c of 1.8 times the doublet spacing d_s. The surface pressure is nondimensionalized by the freestream velocity U_∞ the freestream density ρ_∞ and the heave velocity w_{heave}.

Looking at a compressible heave calculation, specifically the aeroacoustics, Fig. 14 shows the far-field acoustic radiation directivity for a harmonically heaving rectangular wing of aspect ratio 3 with $kC = 1$, $M = 0.1$, and $k_r = 5$. The calculation used a grid of 60×20 smoothed doublets. The pressure is taken 20 chord lengths from the geometric center of the wing. Directivity patterns are taken about the chord, $\theta = 0$ in spherical coordinates, and about the span, $\theta = \pi/2$. In both planes, the far-field acoustic radiation for this case looks like that of an isolated radiating doublet in three dimensions, because the wing is acoustically compact compared to upstream wavelength in the problem. The pressure is reference to the maximum pressure occurring in the field.

Examining a higher frequency and Mach number, Fig. 15 shows the far-field acoustic radiation directivity for a harmonically heaving rectangular wing of aspect ratio 3 with $kC = 5$, $M = 0.5$, and $k_r = 5$. The calculation used a grid of 60×20 smoothed doublets. The pressure is taken 20 chord lengths from the center of the wing. Directivity patterns are taken about the chord, $\theta = 0$ in spherical coordinates, and about the span, $\theta = \pi/2$. In this case, the directivity patterns show more complex behavior than in the previous case. The first directivity pattern shown in Fig. 15 exhibits a nonsymmetric upstream/downstream structure due to the larger convection velocity, and interaction between upstream and downstream waves. The wing is no longer acoustically compact. This is especially evident in the spanwise directivity pattern, $\theta = \pi/2$ (in the bottom of Fig. 15), where a lobe structure is clearly evident.

Consider the response of a rectangular wing to a nonuniform inflow, much like a compressible von Kármán–Sears problem in
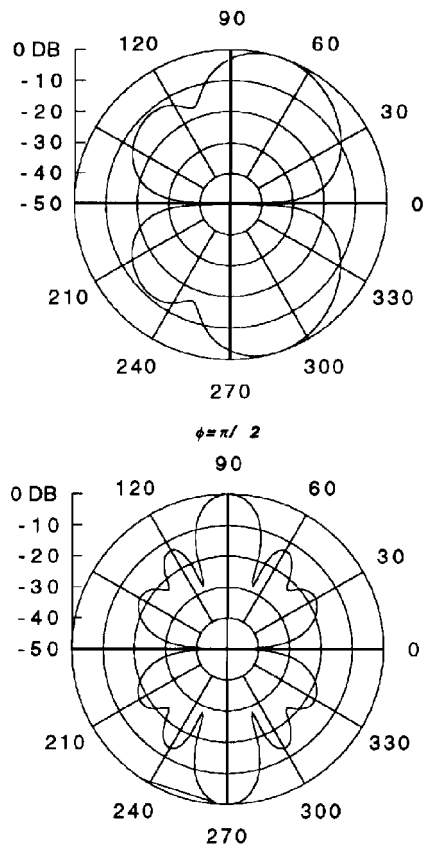
$\phi = \pi/2$

Fig. 15   Directivity pattern for a rectangular wing (aspect ratio 3) subject to harmonic heave: $kC = 5$, $k_r = 5$, $M = 0.5$, $r_c/d_s = 1.8$, $\phi = 0$, **and** $R = 20C$.
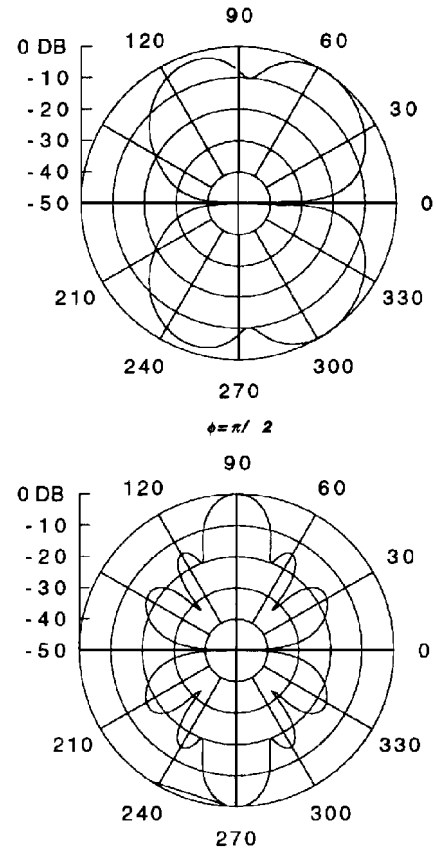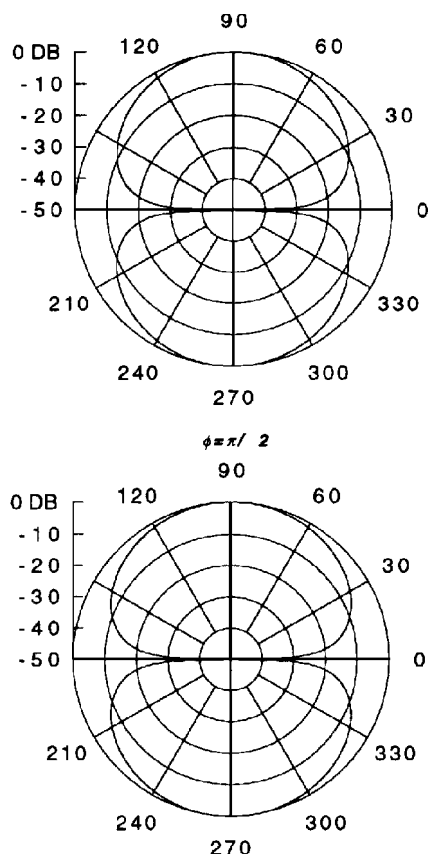
$\phi = \pi/2$

Fig. 16   Directivity pattern for a rectangular wing (aspect ratio 3) subject to a nonuniform sinusoidal gust: $kC = 0.5$, $k_r = 0.5$, $M = 0.5$, $r_c/d_s = 1.8$, $\phi = 0$, **and** $R = 20C$.

$\phi = \pi/2$

Fig. 17   Directivity pattern for a rectangular wing (aspect ratio 3) subject to a nonuniform sinusoidal gust: $kC = 5$, $k_r = 5$, $M = 0.5$, $r_c/d_s = 1.8$, $\phi = 0$, **and** $R = 20C$.

three dimensions. Figure 16 shows the far-field acoustic directivity for an aspect ratio 3 rectangular wing with $kC = 0.5$, $k_r = 0.5$, and $M = 0.5$. The inflow upwash velocity varies sinusoidally. In this calculation, the gust wavelength is approximately 12.5 chord lengths; therefore, the wing is acoustically compact. This is evident in Fig. 16, where the directivity patterns are taken about the chord, $\theta = 0$, and about the span, $\theta = \pi/2$, in which both calculations look like that of an isolated radiating doublet in three dimensions. The calculation used a grid of 60×20 smoothed doublets.

Considering a higher frequency gust, Fig. 17 shows the far-field acoustic directivity for an aspect ratio 3 rectangular wing with $kC = 5$, $k_r = 0.5$, and $M = 0.5$. The calculation used a grid of 60×20 smoothed doublets. The pressure is taken 20 chord lengths from the center of the wing. Directivity patterns are taken about the chord, $\theta = 0$, and about the span, $\theta = \pi/2$. In this case, the directivity patterns show more complex behavior than in the previous case. The first directivity pattern shown in Fig. 15 exhibits a nonsymmetric upstream/downstream structure due to the convection velocity in the problem and interaction between upstream and downstream waves. The wing is no longer acoustically compact. This again is clearly evident in the spanwise directivity pattern, $\theta = \pi/2$ (in the bottom of Fig. 17), where a lobe structure is evident.

V.   Concluding Remarks

A boundary element method based on smoothed fundamental solutions to the convective wave equation has been developed and applied successfully to linear aeroacoustic problems. The formulation is based on a technique called analytical/numerical matching, which offers a fresh point of view on classical lifting surface theory by solving the problem by a fundamentally different means. The ANM approach breaks the problem up into global and local constituent problems that are defined by the physical length scales of the problem and an additional smoothing length scale.

The ANM approach not only offers a unified aeroacoustic method for lifting surface aerodynamics and acoustics but is also free from many of the traditional problems associated with the numerical

solution of singular integral equations. The ANM boundary element formulation leads to accurate solutions and rapid numerical convergence, and it is free from the ambiguity present in many traditional singularity methods.

In practice, ANM is a simple methodology that offers high-resolution aerodynamic and acoustic calculations in the framework of a unified aerodynamic theory.

Acknowledgments

References

[1]Erickson, L. L., "Panel Methods—An Introduction," NASA TP 2995, 1990.

[2]Lifanov, I. K., and Polonskii, I. E., "Proof of the Numerical Method of Discrete Vortices of Solving Singular Integral Equations," *Journal of Applied Mathematics and Mechanics*, Vol. 39, No. 4, 1975, pp. 742–746.

[3]Johnson, F. T., and Rubbert, P. E., "Advanced Panel-Type Influence Coefficient Methods Applied to Subsonic Flows," AIAA Paper 75-50, Jan. 1975.

[4]Johnson, F. T., Rubbert, P. E., and Ehlers, F. E., "A Higher Order Panel Method for General Analysis and Design Applications in Subsonic Flow," *5th International Conference on Numerical Methods in Fluid Dynamics* (Enschede, The Netherlands), Springer–Verlag, Berlin, 1975, pp. 247–253.

[5]Ehlers, F. E., Johnson, F. T., and Rubbert, P. E., "Advanced Panel-Type Influence Coefficient Methods Applied to Subsonic and Supersonic Flows," *LaRC Aerodynamic Analysis Requiring Advanced Computers*, NASA Langley Research Center, 1975, pp. 939–984.

[6]Bliss, D. B., and Epstein, R. J., "A Novel Approach to Aerodynamic Analysis Using Analytical/Numerical Matching," *Proceedings of the AIAA 13th Applied Aerodynamics Conference* (San Diego, CA), AIAA, Washington, DC, 1995.

[7]Bliss, D. B., and Epstein, R. J., "Novel Approach to Aerodynamic Analysis Using Analytical/Numerical Matching," *AIAA Journal*, Vol. 34, No. 11, 1996, pp. 2225–2232.

[8]Epstein, R. J., and Bliss, D. B., "An Acoustic Boundary Element Method Using Analytical/Numerical Matching," *Journal of the Acoustical Society of America*, Vol. 101, No. 1, 1997, pp. 92–106.

[9]Epstein, R. J., and Bliss, D. B., "An Aeroacoustic Boundary Element Method Using Analytical/Numerical Matching," *Proceedings of the 1st Joint CEAS/AIAA Aeroacoustics Conference* (Munich, Germany), Vol. 1, Deutsche Gesellschaft fuer Luft- und Raumfahrt, Bonn, Germany, 1995, pp. 491–500.

[10]Epstein, R. J., and Bliss, D. B., "Free Vortex Calculations Using Analytical/Numerical Matching with Solution Pyramiding," *AIAA Journal*, Vol. 33, No. 5, 1995, pp. 894–903.

[11]Quackenbush, T. R., Lam, C.-M., and Bliss, D. B., "Vortex Methods for the Computational Analysis of Rotor/Body Interaction," *Journal of the American Helicopter Society*, Vol. 39, No. 4, 1994, pp. 14–24.

[12]Bliss, D. B., and Epstein, R. J., "Free Vortex Problems Using Analytical/Numerical Matching and Solution Pyramiding," AIAA Paper 94-2199, June 1994.

[13]Bliss, D. B., and Miller, W. O., "Efficient Free Wake Calculations Using Analytical/Numerical Matching," *Journal of the American Helicopter Society*, Vol. 38, No. 2, 1993, pp. 878, 879.

[14]Epstein, R. J., "A Novel Boundary Element Method Using Analytical/ Numerical Matching for Aerodynamics, Acoustics and Aeroacoustics," Ph.D. Thesis, Dept. of Mechanical Engineering and Materials Science, Duke Univ., Durham, NC, April 1996.

[15]Garrick, I. E., *Nonsteady Wing Characteristics, Aerodynamics of Aircraft Components of High Speed*, Vol. 8, Princeton Univ. Press, Princeton, NJ, 1957, Sec. F.

[16]Ashley, H., and Landahl, M., *Aerodynamics of Wings and Bodies*, Dover, Mineola, NY, 1965.

[17]Garrick, I. E., "On Moving Sources in Nonsteady Aerodynamics and in Kirchhoff's Formula," *Proceedings of the First U.S. National Congress of Applied Mechanics*, Chicago, IL, 1951.

[18]Morse, P. M., and Feshbach, H., *Methods of Theoretical Physics*, McGraw–Hill, New York, 1953.

[19]Kellogg, O. D., *Foundations of Potential Theory*, Dover, Mineola, NY, 1953.

[20]Baker, B., and Copson, E., *The Mathematical Theory of Huygens' Principle*, Chelsea, New York, 1987.

[21]Das, A., "On Disturbance Field of Moving Singularities in Aerodynamics and Aeroacoustics," European Space Agency, TR ESA-TT-570, 1979; also DFVLR-FB-78-16.

[22]Das, A., "Wave Propagation from Moving Singularities and a Unified Exposition of the Linearized Theory for Aerodynamics and Acoustics," DFVLR, TR DFVLR-FB-84-17, 1984.

[23]Larmor, J., "On the Mathematical Expression of the Principle of Huygens," *Proceedings of the London Mathematical Society*, Vol. 2, No. 1, 1903, pp. 1–13.

[24]Morino, L., "A General Theory of Unsteady Compressible Potential Aerodynamics," NASA, TR CR 2464, Dec. 1974.

[25]Beale, J. T., and Majda, A., "High Order Accurate Vortex Methods with Explicit Velocity Kernels," *Journal of Computational Physics*, Vol. 58, No. 2, 1985, pp. 188–208.

[26]Jones, R. T., and Cohen, D., *Aerodynamics of Wings at High Speeds*, Vol. 7, Aerodynamics of Aircraft Components at High Speeds, Princeton Univ. Press, Princeton, NJ, 1957.

[27]Van Dyke, M., *Perturbation Methods in Fluid Mechanics*, Parabolic, Stanford, CA, 1975.

[28]Jones, R. T., *Wing Theory*, Princeton Univ. Press, Princeton, NJ, 1990.

[29]Theodorsen, T., "General Theory of Aerodynamics Instability and the Mechanism of Flutter," NACA, TR R-496, 1935.

[30]Von Kármán, T., and Sears, W. R., "Airfoil Theory for Nonuniform Motion," *Journal of the Aeronautical Sciences*, Vol. 5, No. 10, 1938.

[31]Dowell, E. H., *A Modern Course in Aeroelasticity*, Kluwer Academic, Dordrecht, The Netherlands, 1989.